

Run-away transition to turbulent strong-field dynamo

A. Guseva^{1,2,*}, L. Petitdemange¹, and S. M. Tobias²

¹LERMA, l'Observatoire de Paris, Sorbonne Université, Université PSL, CNRS, 75014 Paris, France

²Department of Applied Mathematics, University of Leeds, Leeds LS2 9JT, UK

*Corresponding author: anna.guseva@obspm.fr

Abstract

Planets and stars are able to generate coherent large-scale magnetic fields by helical convective motions in their interiors. This process, known as hydromagnetic dynamo, involves nonlinear interaction between the flow and magnetic field. Nonlinearity facilitates existence of bi-stable dynamo branches: a weak field branch where the magnetic field is not strong enough to enter into the leading order force balance in the momentum equation at large flow scales, and a strong field branch where the field enters into this balance. The transition between the two with enhancement of convection can be either subcritical or supercritical, depending on the strength of magnetic induction. In both cases, it is accompanied by topological changes in velocity field across the system; however, it is yet unclear how these changes are produced. In this work, we analyse transitions between the weak and strong dynamo regimes using a data-driven approach, separating different physical effects induced by dynamically active flow scales. Using Dynamic Mode Decomposition, we decompose the dynamo data from direct numerical simulations into different components (modes), identify the ones relevant for transition, and estimate relative magnitudes of their contributions Lorentz force and induction term. Our results suggest that subcritical transition to a strong dynamo is facilitated by a subharmonic instability, allowing for a more efficient mode of convection, and provide a modal basis for reduced-order models of this transition.

1 Introduction

The flow dynamics in planetary cores can be greatly affected by large-scale magnetic fields, generated by helical convective motions in a process known as hydromagnetic dynamo [1]. In the context of stability theory, dynamo may arise as a kinematic instability of non-magnetic convection when magnetic induction is larger than magnetic diffusion so that a certain ratio between them, critical magnetic Reynolds number Rm , is achieved. This condition is fulfilled for planetary flows with their extremely large length scales; $Rm \sim O(10^3)$ for geodynamo [2]. An observable manifestation of planetary dynamos are magnetic torsional waves detected in secular variations of the Earth magnetic field [3, 4] and Jupiter luminosity [5]. They arise when magnetic tension enters in the dominant balance with buoyancy (Archimedean) and the Coriolis force in the momentum equation, so-called MAC balance [6]. This force balance, corresponding to a "strong"-field dynamo, constrains magnetic field to the Taylor state. In this state, the azimuthal component of magnetic tension, averaged over cylindrical surfaces parallel to rotation axis, tends to zero, because all other forces in azimuthal direction are either zero or negligible [7]. Considerable progress to obtain planetary-like Taylor state dynamos was made through analysing mean-field dynamos driven by a parametrized electromotive force [8] and using adjoint-based optimization [9].

At the same time, self-consistent numerical models of planetary dynamos, driven solely by convection, were able to reproduce predominantly dipolar magnetic field topology both in Boussinesq and anelastic models [10, 11]. However, realistic planetary parameter regimes are computationally unachievable, because the rotation time scale is much faster compared to the time scale of viscous or magnetic dissipation. The ratio between the two time scales, Ekman number, is estimated to be $E = 10^{-14}$ for the Earth, 10^{-16} for Jupiter, and 10^{-17} for Saturn [12], in contrast to 10^{-6} accessible

to the state-of-art direct numerical simulations [13]. It was proposed to reduce the Ekman number and the magnetic Prandtl number Pm , the ratio between viscosity and magnetic diffusivity, simultaneously to keep the ratio of time scales in simulations as close as possible to the Earth-like regime [2, 14–16]. Even then, simulations result in the dominant quasi-geostrophic (QG) balance between the Coriolis force and pressure gradient at the largest flow scales, reproducing MAC balance only at the second order, after the geostrophic or gradient components of forces are removed [15, 17]. The flows in QG force balance, aligned along the rotation axis due to the Taylor-Proudman theorem, can also support steady large-scale fields, although in a “weak”-field regime where the magnetic Lorentz torque is balanced by viscous force [18]. Such “weak”-field dynamos are less likely to excite magnetic waves observed in planets because the restoring magnetic Lorentz force would be too weak.

Another strategy to reach MAC regime is to decrease magnetic diffusivity as compared to viscosity while keeping E relatively high, i.e. to increase the magnetic Prandtl number [19, 20]. Weaker magnetic dissipation allows to obtain stronger magnetic fields and stronger Lorentz force. This approach works well close enough to the onset of convection, because simultaneous increase in convective forcing also increases inertia and may lead to dipole breakdown and multipolar magnetic fields [21], unless the field is strong enough to extend the stability domain of dipolar dynamos [22]. However, it is computationally less expensive and allows to explore a range of different parameter regimes of “weak” and “strong”-field dynamos, and transitions between them. At relatively low Pm , these transitions are gradual, or supercritical: mildly chaotic, multi-modal turbulent convection excites weak axisymmetric dynamo mode that gradually builds up its energy in the saturated state with enhancement of convective forcing [20]. Through nonlinear Lorentz force, it reduces the level of turbulence in the flow or even suppresses it to laminar, one-mode convection. On the other hand, at large Pm , a “weak” dynamo is easily excited by near-critical convectively unstable flow modes, even when convection is not turbulent. In this case, an abrupt, subcritical transition to turbulent yet predominantly dipolar “strong”-field dynamo can take place when convective forcing is only slightly increased. Such transitions are essentially nonlinear processes of interaction between the field and the flow through the Lorentz force and induction term, and can be relevant for developing dynamos in young planets or failed dynamos in formerly magnetized planets like Mars [23]. It is yet not well understood how the corresponding topological changes in the magnetic field and velocity, affect the dynamo action, and what triggers turbulence in the case of abrupt, subcritical transitions at high Pm .

In this work, we aim to fill this gap through analysis of subcritical transition from the weak to strong dynamo, combining direct numerical simulations (DNS) and a data-driven approach (section 2). In complex three-dimensional dynamos, a large number of degrees of freedom is required to represent the flow and field in the DNS. We employ a data-driven analysis method, Dynamic Mode Decomposition (DMD), to represent physical processes behind the transition in a more compact way and to identify principal dynamical components in the data from dynamo simulations, as described in section 3. DMD seeks for the closest linear approximation to a nonlinear system [24], and was recently used to identify small- and large-scale periodic dynamics in one-dimensional dynamo models [25] and quasi-Keplerian magnetohydrodynamic turbulence [26]. In section 4 we decompose the dynamo flow into convective Rossby wave and its subharmonic, appearing during transition. Section 5 describes how nonlinear interactions between the flow and the field are affected by presence of these structures. Finally, we analyse the breakdown of the subharmonic mode to a chaotic state through a secondary instability (section 6) and discuss our results in section 7.

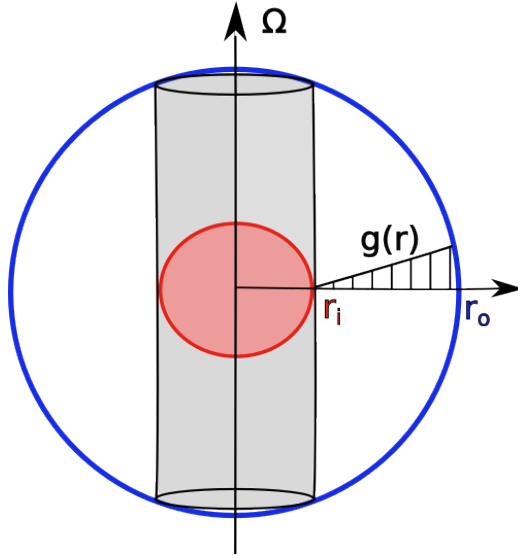


Figure 1: The computational domain. Conducting fluid is confined between two co-rotating spheres and Boussinesq approximation is assumed, with gravity g linearly proportional to the spherical radius. The grey area indicates the tangent cylinder, the imaginary surface circumscribing the inner sphere.

2 Dynamo equations and methods

We solve coupled equations for velocity \mathbf{u} , magnetic field \mathbf{B} and temperature T for incompressible fluid in the Boussinesq approximation in a rotating spherical shell,

$$\begin{aligned}
 E\left(\frac{\partial \mathbf{u}}{\partial t} + \mathbf{u} \cdot \nabla \mathbf{u}\right) &= -\nabla P - 2\mathbf{z} \times \mathbf{u} + Ra \frac{\mathbf{r}}{r_o} T + \frac{1}{Pm} (\nabla \times \mathbf{B}) \times \mathbf{B} \\
 \frac{\partial \mathbf{B}}{\partial t} &= \nabla \times (\mathbf{u} \times \mathbf{B}) + \frac{1}{Pm} \nabla^2 \mathbf{B} \\
 \frac{\partial T}{\partial t} + \mathbf{u} \cdot \nabla T &= \frac{1}{Pr} \nabla^2 T, \\
 \nabla \cdot \mathbf{B} &= 0.
 \end{aligned} \tag{1}$$

Equations (1) are solved in spherical coordinates (r, θ, ϕ) ; we also introduce cylindrical coordinate system (s, ϕ, z) aligned with the axis of rotation, for data analysis. Convection is driven by an imposed temperature difference $\Delta T = T_i - T_o$ between the cooler outer sphere of radius r_o and the hotter inner sphere of radius $r_i = 0.35r_o$. Figure 1 illustrates the computational setup of two concentric spheres, rotating with constant angular velocity Ω and containing conducting fluid with density ρ , viscosity ν , thermal diffusivity κ and magnetic diffusivity η . The grey area denotes the tangent cylinder, an imaginary cylindrical surface around the inner sphere with cylindrical radius $s = r_i$. The equations are non-dimensionalized with ΔT , the gap width between the spheres $d = r_o - r_i$, viscous time d^2/ν , and the magnetic scale $(\rho\mu\eta\Omega)^{1/2}$. The Ekman number was set to $E = \nu/\Omega d^2 = 10^{-4}$, the magnetic Prandtl number to $Pm = \nu/\eta = 12$, and the thermal Prandtl number to $Pr = \nu/\kappa = 1$. The modified Rayleigh number $Ra = \alpha g_0 \Delta T d / \nu \Omega$, where α is thermal expansivity and g_0 is gravitational acceleration at r_o , controls convection strength. Ra was varied in the parameter regime where transitions between weak- and strong-field dynamo topologies were previously observed [20]. Equations (1) were solved numerically with pseudospectral DNS code PaRoDy [27], with no-slip boundary conditions for velocity and insulating boundary conditions for magnetic field on both spheres. In spectral space, the flow variables were represented by spherical harmonics with azimuthal periodicity, or wavenumber, m and spherical degree l . We used the $N_r = 240$ radial points and $N_\phi, N_\theta = 72$ spherical harmonics with 3/2 dealiasing rule.

Dynamic Mode Decomposition is a data-driven approach for identification of coherent structures in dynamical systems like (1) [24]. Nonlinear magnetohydrodynamic equations (1) evolve state vector

$\mathbf{q}(t) = (\mathbf{u}, \mathbf{B}, T)$ of the flow variables at a given point $\boldsymbol{\mu}$ in the parameter space,

$$\frac{d\mathbf{q}}{dt} = f^{\text{nonlinear}}(\mathbf{q}, t, \boldsymbol{\mu}), \quad \boldsymbol{\mu} = (Ra, E, Pm, Pr). \quad (2)$$

According to Koopman theory [28], a generic nonlinear system (2) can be equivalently represented with a linear operator \mathcal{K} , propagating in time an infinite number of flow observables $f(\mathbf{q})$ as $f(\mathbf{q})(t_{k+1}) = \mathcal{K}f(\mathbf{q})(t_k)$ at each moment in time t_k . The eigenfunctions and eigenvalues of \mathcal{K} correspond thus to the dominant flow components and their evolution in time. Dynamic Mode Decomposition approximates the Koopman operator using matrices of DNS data,

$$Q = [q_1, q_2, \dots, q_{k-1}], \quad Q' = [q_2, q_3, \dots, q_k], \quad Q' = \mathcal{A}Q \quad (3)$$

collected at times t_1, t_2, \dots, t_k [29, 30]. In essence, matrix A is a data-driven linearization of the system (1) about its nonlinear state, obtained from simulations or measurements. For computational stability, it is practical to get first its reduced representation A_r in the space of principal orthogonal modes Φ_r of the data, using singular value decomposition of the data matrix $Q = \Phi_r \Sigma_r V_r^*$ and further linear matrix transformations,

$$Q' \approx \mathcal{A} \Phi_r \Sigma_r V_r^*, \quad \Phi_r^* \mathcal{A} \Phi_r = \Phi_r^* Q' V_r \Sigma_r^{-1} = \mathcal{A}_r. \quad (4)$$

The elements of matrices Σ and V correspond to the energy and temporal evolution of the modes Φ , respectively. The number of retained POD modes, model rank r , is a parameter of the DMD approximation, setting the number of linearly independent components. In this work it was set to retain 99% of the energy in each dynamo variable in (1). The eigenvalues and eigenvectors of A_r are calculated and then reconstructed from r -dimensional space as

$$\mathcal{A}_r \tilde{\psi} = \lambda \tilde{\psi}, \quad \psi = \frac{1}{\lambda} Q' V_r \Sigma_r^{-1} \tilde{\psi}, \quad \omega = \ln(\lambda) / \Delta t. \quad (5)$$

In the following, we will refer to the eigenfunctions ψ as DMD modes and to eigenvalues ω as DMD eigenvalues. The real and imaginary parts of ω , $\Re(\omega)$ and $\Im(\omega)$, correspond to modal growth rates and frequencies, respectively. See Schmid [24], Tu et al. [29], Arbabi and Mezic [30], Schmid [31] for more details on the DMD algorithm and the underlying Koopman theory.

3 Transition between the weak and strong dynamo in simulations

Figure 2(a) summarizes results of our simulations of the weak and strong dynamos, based on rms value of the total magnetic field in a statistically steady state. The shaded region highlights co-existence of the two regimes in the range of $Ra \in [150, 165]$. Thus, if the flow is initialized with a small random or dipolar initial perturbation in magnetic field, it will remain on the weak branch until $Ra \approx 165$, with the rms amplitude of magnetic field remaining small. Further increase in convective forcing results in magnetic energy increase and transition of the flow to the upper, strong-field branch. Figure 2(b) depicts the evolution of kinetic and magnetic energy during such transitions for $Ra = 170$ and $Ra = 180$, and two different weak-field initial conditions at $Ra = 160$ and $Ra = 165$, respectively. Initially, the system settles down into a weak-field solution ($t < 1.3$); it is characterized by predominantly dipolar axisymmetric field inside the tangent cylinder perturbed by the convective thermal Rossby wave near equator (figure 2c, left). In this regime, the flow consists of a single convective mode and is constrained vertically through Taylor-Proudman theorem. The axisymmetric zonal flow,

$$V_\phi = \langle u_\phi \rangle_\phi, \quad (6)$$

where brackets denote average over ϕ , is weak in this regime. It is formed by retrograde jets near both the tangent cylinder and equator (figure 2d, left), separated by prograde flow regions. This initial state is unstable, and both magnetic and kinetic energies gradually increase, saturating into another quasi-steady solution, active when $t \in [1.5, 2.0]$. This solution is also unstable, and after a rapid run-away growth in both kinetic and magnetic energies, the flow transitions to a chaotic dynamo state

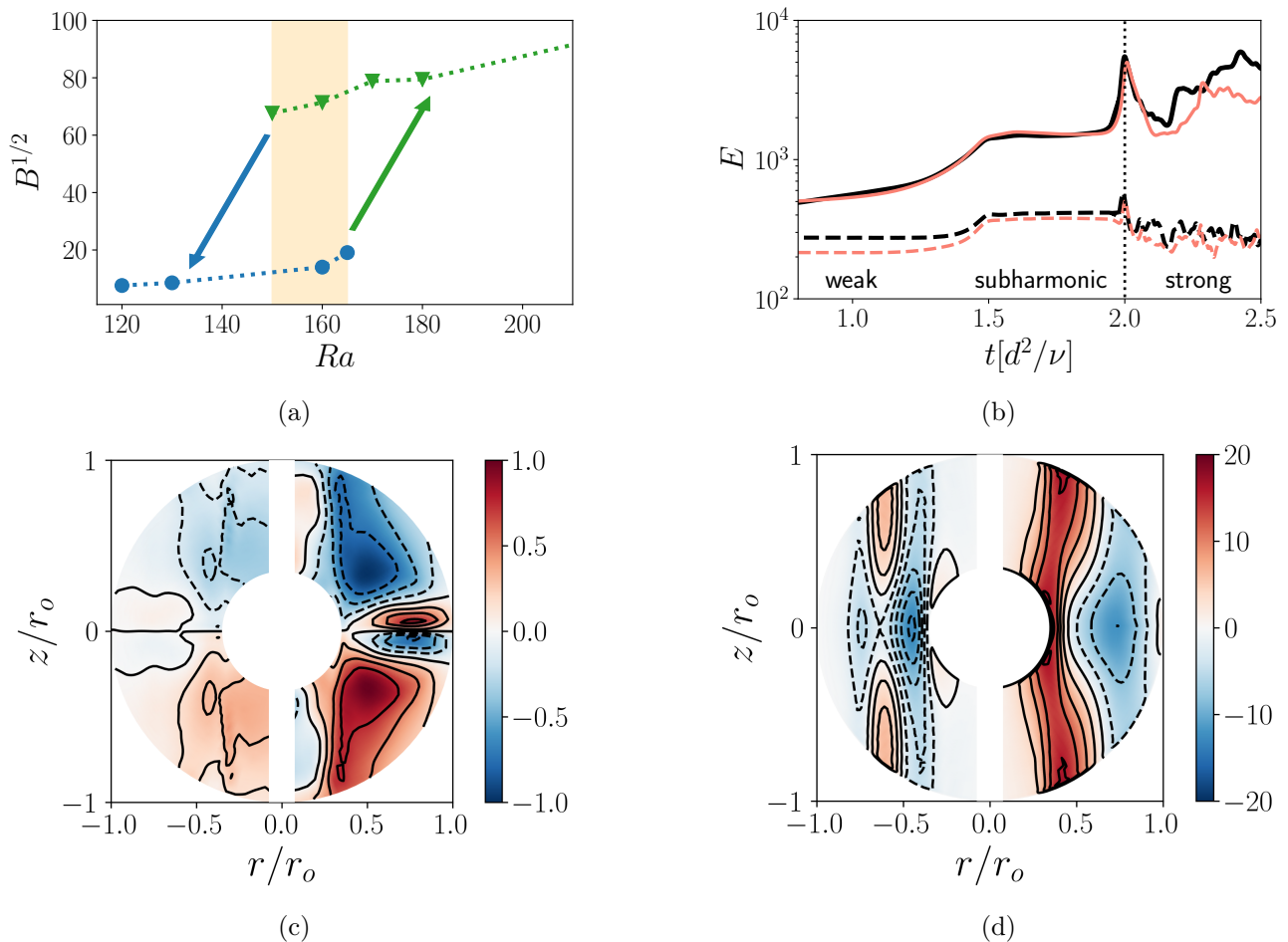


Figure 2: (a) Rms amplitude of magnetic field of the weak (blue circles) and strong dynamos (green triangles); shaded region denotes co-existence of the two branches. Green arrow indicates transition from the weak to strong branch (panel b) and the blue arrow inverse transition (figure 8b). (b) Kinetic (dashed) and magnetic energy (solid) during transition. In black: $Ra = 180$, initial condition of weak dynamo at $Ra = 165$. In red: $Ra = 170$, initial condition at $Ra = 160$. Time series are shifted in time for comparison so that transition to strong-field dynamo takes place at $t = 2$ (dotted line). (c) Radial component of axisymmetric magnetic field B_r , averaged over ϕ and time, in the weak (left) and the strong-field regime (right). (d) The same as (c) but for the axisymmetric zonal flow $V_\phi = \langle u_\phi \rangle_\phi$.

driven by turbulent convection, i.e. the strong dynamo branch in figure 2(a). The magnetic field is still predominantly dipolar, with a strong axisymmetric $l = 1$ component (figure 2c, right), yet now this field is predominantly outside of the tangent cylinder. In this regime, convection is multi-modal, kinetic energy is much smaller than magnetic (figure 2b), and a strong prograde zonal flow develops (figure 2d, right) along the tangent cylinder. The larger Ra , the less time the flow spends in the vicinity of the weak-field state, however, the overall time and evolution path taken by this transition remain independent of Ra , or different weak-field initial conditions. Conversely, when a dynamo simulation is initialized with a strong-field chaotic state, it remains on the strong-field dynamo branch as Ra is gradually reduced. Only when convective forcing decreases beyond the left border of the bistable region in figure 2(a), the flow gradually relaxes into a weak-field state, losing energy in chaotic components and saturating to the dominant convective mode. The energy for the run with $Ra = 120$ is slowly decaying, so the dynamo is potentially not supported by convection for $Ra \leq 120$.

In this work, we will analyse three different simulations with similar transition scenarios, the first one at $Ra = 170$ and initial conditions at $Ra = 160$, the second at $Ra = 180$, with the same initial conditions, and the third one again at $Ra = 180$ but with the initial state at $Ra = 165$. We initialize our simulations with a saturated weak-field dynamo at lower Ra and then slightly increase convective forcing, thus perturbing the flow. We collect flow data for these three cases during the time interval in

figure 2(b), and analyse separately the four stages of transition: weak dynamo, transient high-energy state, run-away increase in dynamo energy, relaxation to a chaotic strong-field dynamo.

4 DMD modes and their evolution during transition

We perform DMD of different components of DNS dynamo data in the weak ($t < 1.3$) and transient regimes ($1.3 < t < 2.0$) separately, using the algorithm described in section 2. Since temperature, magnetic and velocity fields are related through nonlinear terms in (1), all the flow variables contain some contribution from the dominant flow components due to nonlinear quadratic interactions in the flow. We thus show the typical spectrum of DMD eigenvalues for temperature T in figure 3(a), colored by their best-fit magnitudes [32]. During the weak phase, the dynamo has only two principal modes: a convective Rossby wave, resulting from vertical alignment of convective cells due to rotation, and the mean flow modes with $\Im(\omega) = 0$. The Rossby wave has a frequency of $\Im(\omega) \approx 60$ for $Ra = 180$ and $\Im(\omega) \approx 80$ for $Ra = 170$, and comprises five pairs of convective cells in azimuthal direction, corresponding to the azimuthal wavenumber $m = 5$. Figure 3(c) illustrates the spatial shape of this mode for the radial component of magnetic field, antisymmetric with respect to the equator. Convective cells of this structure are inclined and rotate in the direction of global rotation. Rossby waves, driven by convective temperature gradient, generate mean dipolar magnetic field component in B_r , B_θ , and B_ϕ . This is identified by DMD as the mean-field mode with frequency of $\Im(\omega) = 0$, which has the strongest amplitude in the magnetic field both in weak and transient regimes. Its spatial structure (figure 3b, left) correlates well with the mean field (figure 2c, left). In temperature, convective mixing by the Rossby wave also results in the mean mode with $\Im(\omega) = 0$ (figure 3a), corresponding to deformation and flattening of initially linear mean temperature profile. The $\Im(\omega) = 0$ contributions to u_r and u_θ , i.e. meridional flows, are absent or very weak. The $\Im(\omega) = 0$ component of u_ϕ , corresponding to zonal flow V_ϕ , represents less than 10% of the flow energy in the weak-field regime, very small amount compared to the Rossby waves.

In the transient subharmonic regime, the Rossby wave becomes less coherent and is now identified by DMD as damped (figure 3a); instead, a subharmonic mode of the Rossby wave overtakes the dynamics. It has also azimuthal periodicity of $m = 5$ but half the frequency, $\Im(\omega) = 30$, and thus two times slower rotation in azimuthal direction. Figure 3(d) shows a meridional slice of this mode for B_r , where the outer convective cells have expanded over the equatorial area. In the vertical direction, a local maximum appeared at the tangent cylinder, where the mode changes sign. The contours of this structure are less aligned with the direction of rotation. The subharmonic component drives a strong zonal flow (figure 3b, right), detectable in the DMD spectrum of u_ϕ (not shown here). This zonal flow is inverted in comparison to the weak state (figure 2d, left) and take form of strong prograde jet at the tangent cylinder and weaker retrograde jet at the equator. The development of zonal flow is accompanied by topological changes in magnetic field. Strong V_ϕ promotes toroidal field $\langle B_\phi \rangle_\phi$; to satisfy divergence-free condition, axisymmetric $\langle B_r \rangle_\phi$ and $\langle B_\theta \rangle_\phi$ also adjust. The shape of $\Im(\omega) = 0$ mode of magnetic field changes considerably (figure 3b, middle), so that The local maxima in B_ϕ move from the regions inside the tangent cylinder towards its boundary. Magnetic field becomes concentrated at the tangent cylinder, and the regions inside it become stagnant and contain less magnetic flux than in the weak-field state. The remaining component of the DMD spectrum in figure 3(a) with higher frequency $\Im(\omega) > 100$ corresponds to quadratic interaction of the Rossby wave with itself and thus has azimuthal periodicity of $m = 10$, yet preserving its vertical structure. When the subharmonic is dominant, similar modes corresponding to quadratic nonlinear interactions of subharmonic flow components also appear (see an additional $\Im(\omega) \approx 60$ mode in the transient dynamo spectrum in figure 3a).

Further insight on the dynamical behaviour of the mean mode, Rossby and subharmonic waves can be obtained by projecting the DNS dynamo data onto the identified above modal basis, using oblique least-squares projection (see [25] for more details). This procedure gives instantaneous coefficients of the modes, and allows to follow their temporal evolution during all four phases of transition. Figure 4(a) shows how the absolute values of the Rossby wave coefficient decrease both in B_ϕ and u_ϕ , while the amplitude of the subharmonic grows and saturates for a limited period of time in the transient state,

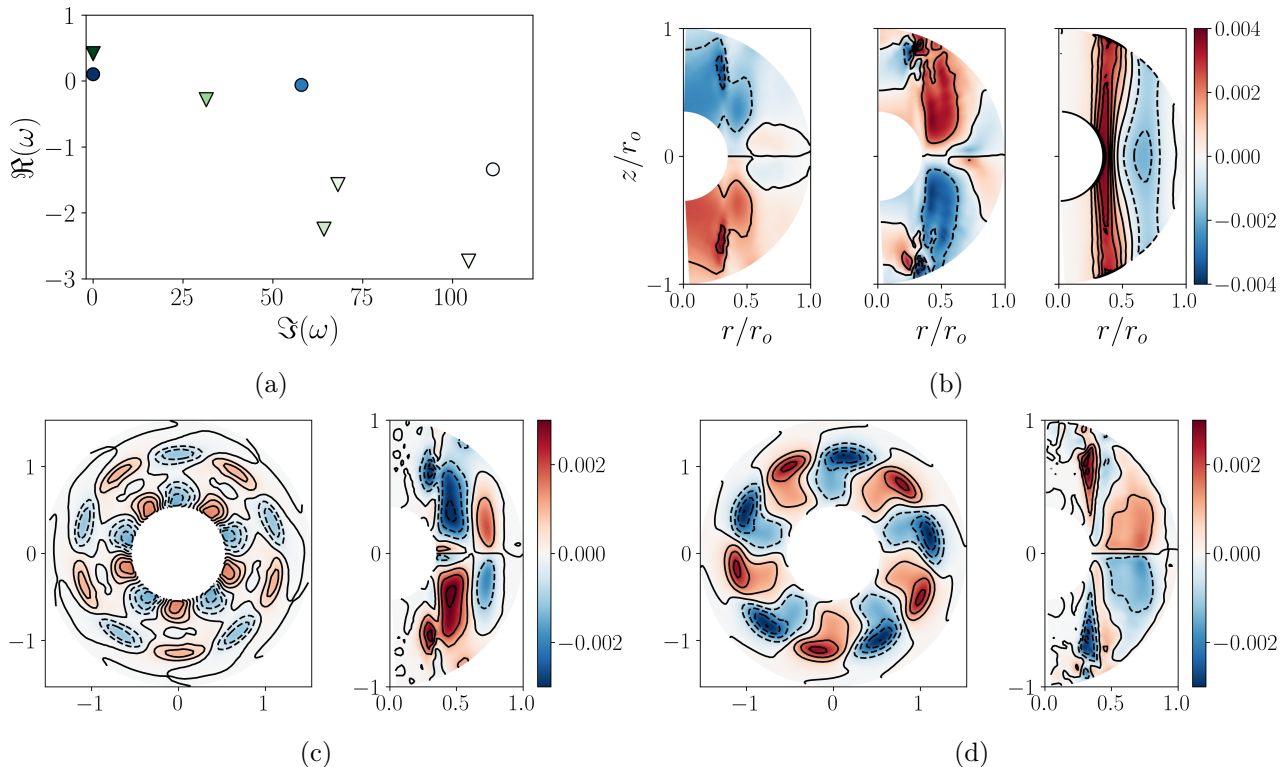


Figure 3: (a) DMD spectrum of temperature T . Blue circles, the “weak” phase; green triangles, transition to strong dynamo regime. (b) Left, the “mean” mode of weak magnetic field B_r , with frequency $\Im(\omega) = 0$; middle, same mode but during transition; right, the “mean” mode of azimuthal velocity component u_ϕ , of the transient subharmonic state. (c) Equatorial and latitudinal cross-sections of the convective Rossby wave, $\Im(\omega) = 60$. (d) Subharmonic mode with $\Im(\omega) = 30$, identified during transition. $Ra = 180$, initial conditions at $Ra = 160$.

with energy exchange between the two during this transition. The Rossby wave loses its coherence, and becomes nearly extinct in components of magnetic field, but retains some energy in the flow. The amplitude of the mean mode of temperature grows by a factor of 1.5, with further flattening of mean temperature profile in the bulk of the flow and more efficient heat transport (figure 4b). The zonal flow mode grows nearly by 90%, correlated with the growth of the mean toroidal field B_ϕ . Since the zonal flow is weak in the weak dynamo state (figures 2d,f), we can ignore spatial reconfiguration of V_ϕ as the subharmonic grows. It is partially accounted for by the change of sign of the modal coefficient of the corresponding subharmonic mode, when the flow in the weak-field regime is projected on it.

5 Evolution of forces during transition

5.1 Modal contribution to induction and Lorentz forces

In this section, we estimate the contribution of the Rossby and subharmonic modes to the induction term and Lorentz force from equations (1),

$$\mathbf{F}_I = \nabla \times (\mathbf{u} \times \mathbf{B}), \quad \mathbf{F}_L = \frac{1}{Pm} (\nabla \times \mathbf{B}) \times \mathbf{B}, \quad (7)$$

responsible for nonlinear interactions between the flow and the field, and leading to the dynamo saturation. Reconstructing velocity and magnetic fields from the modes (figures 3b-d) and their temporal coefficients (figure 4), we decompose velocity and magnetic fields as

$$\mathbf{u} = \mathbf{u}^M + \mathbf{u}^{RW} + \mathbf{u}^{SW} + \dots, \quad \mathbf{B} = \mathbf{B}^M + \mathbf{B}^{RW} + \mathbf{B}^{SW} + \dots \quad (8)$$

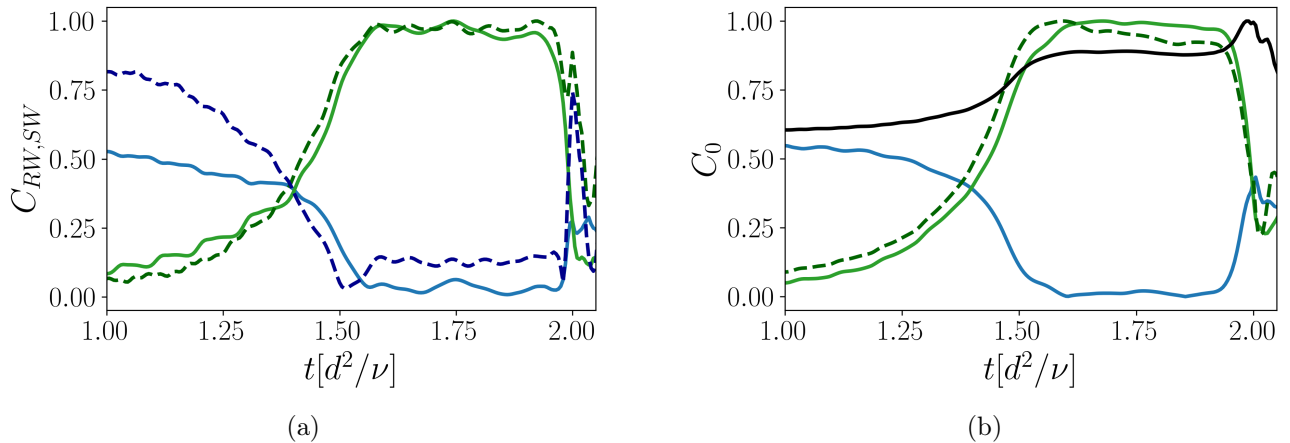


Figure 4: Absolute values of modal coefficients. (a) In blue, Rossby wave obtained in the weak regime, in green, its subharmonic. Solid lines, B_ϕ ; dashed, u_ϕ . (b) Coefficients of the mean modes with $\Im(\omega) = 0$. Solid blue (green), from B_ϕ in the weak (transient) regime. Dashed green, from u_ϕ in the transient subharmonic state. In black, the coefficient of mean-field mode of temperature. $Ra = 170$, initial conditions at $Ra = 160$.

Here M denotes the mean mode, which is equivalent to the zonal flow V_ϕ in velocity field, RW denotes the Rossby wave, and SW its subharmonic. The corresponding expansion for induction term,

$$\begin{aligned} \mathbf{F}_I = & \nabla \times (\mathbf{u}^M \times \mathbf{B}^M) + \nabla \times (\mathbf{u}^{RW} \times \mathbf{B}^{RW}) + \nabla \times (\mathbf{u}^{SW} \times \mathbf{B}^{SW}) \\ & + \nabla \times (\mathbf{u}^M \times \mathbf{B}^{RW}) + \nabla \times (\mathbf{u}^{RW} \times \mathbf{B}^M) + \nabla \times (\mathbf{u}^M \times \mathbf{B}^{SW}) \\ & + \nabla \times (\mathbf{u}^{SW} \times \mathbf{B}^M) + \nabla \times (\mathbf{u}^{SW} \times \mathbf{B}^{RW}) + \nabla \times (\mathbf{u}^{RW} \times \mathbf{B}^{SW}) + \dots, \end{aligned} \quad (9)$$

isolates interaction of different velocity and magnetic structures: mean, Rossby and subharmonic wave with themselves, interaction of the mean with Rossby or subharmonic mode, and interaction of the Rossby wave and its subharmonic.

Figure 5(a) shows the rms value of the strongest terms from expansion (9) to the total induction, integrated over the computational domain,

$$|F_I|^V = \left[(1/V) \int_V (F_{I,r}^2 + F_{I,\theta}^2 + F_{I,\phi}^2) dV \right]^{1/2}, \quad (10)$$

as a function of time. During the weak dynamo phase, induction has the largest contribution from the interaction of the Rossby wave with the mean magnetic field (dashed line), adding a perturbation to magnetic field with the same azimuthal periodicity of $m = 5$ and frequency of the Rossby wave through triadic interaction $(\mathbf{u}^M, \mathbf{B}^{RW}, \mathbf{B}^{RW})$ in the quadratic terms (7). The second largest component is the interaction of this perturbation with the Rossby wave in the flow (solid line), feeding back into the mean dipole component of magnetic field through $(\mathbf{u}^{RW}, \mathbf{B}^{RW}, \mathbf{B}^M)$ or its second harmonic with $\Im(\omega) = 2\Im(\omega)_{RW}$ flow component, also detected by DMD (see figure 3a). This interaction can be interpreted as α -effect, an electromotive force generating large-scale magnetic fields from correlated fluctuations of the flow and field in the framework of the mean-field dynamo theory [1, 33]. Since it appears in all components of induction, and the zonal flows are weak, the weak-field state is essentially an α^2 -dynamo [34, 35].

When the subharmonic mode begins to grow and overwhelms the Rossby wave, these induction components decrease. Instead, the interaction of the subharmonic with itself becomes larger than its weak-field counterpart, indicating enhancement of induction. Since the Rossby wave component in magnetic field is weak in this regime, it appears that the triads of $(\mathbf{u}^{SW}, \mathbf{B}^{SW}, \mathbf{B}^M)$ are preferred by the flow over $(\mathbf{u}^{SW}, \mathbf{B}^{SW}, \mathbf{B}^{RW})$. Consistent with that, the dominant contributions to induction come from interaction of the subharmonic in the flow with the mean magnetic field, which can be again interpreted as α -effect, and the subharmonic in the field with the enhanced zonal flow mode u^M , a proxy for Ω -effect of toroidal field generation by differential rotation. Both these interactions transfer

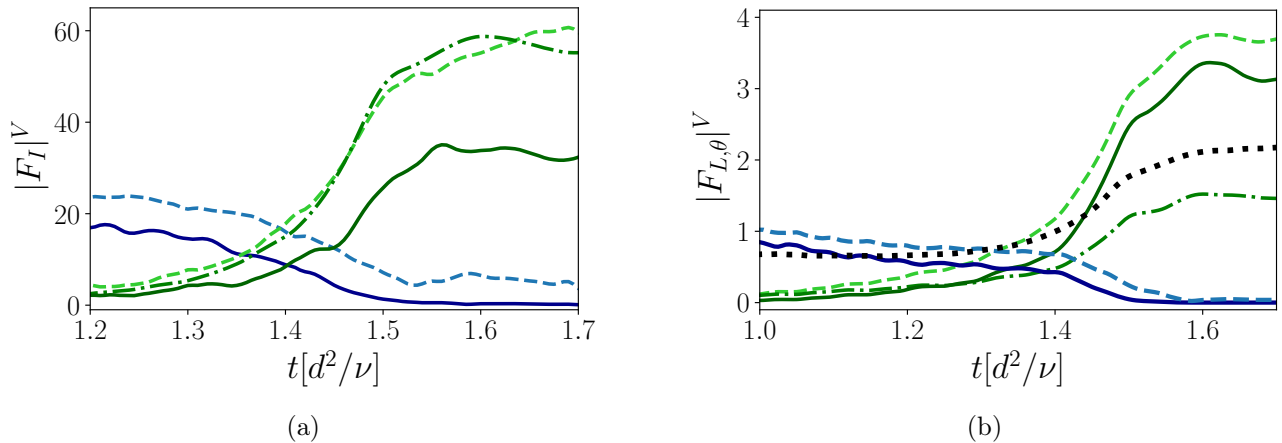


Figure 5: (a) Modal contributions to the integrated induction term $|F_I|^V$ (10). Solid, interaction of $u^{RW(SW)}$ with $u^{RW(SW)}$; dashed, interaction of $u^{RW(SW)}$ with B^M ; dashdotted, interaction of u^M with $B^{RW(SW)}$. Blue color corresponds to the Rossby wave and green color to the subharmonic. (b) Volume-integrated θ -component of the Lorentz force (11). Notation as in (a); the black dotted line represents interaction of B^M with the current induced by it, $\nabla \times \mathbf{B}^M$. M denotes the mean mode, RW denotes the Rossby wave, and SW its subharmonic. $Ra = 180$, initial conditions at $Ra = 165$.

energy to the subharmonic wave and reinforce it, and $\alpha - \Omega$ dynamo becomes the principal dynamo mechanism during the transient subharmonic state.

The expansion for the Lorentz force \mathbf{F}_L is derived similarly to equation (9) as a sum of products of different magnetic components in (8) with induced by them currents $\nabla \times \mathbf{B}^M$, $\nabla \times \mathbf{B}^{RW}$, $\nabla \times \mathbf{B}^{SW}$. Figure 5(b) shows the volume integral of the θ -component of the Lorentz force,

$$|F_{L,\theta}|^V = \left[(1/V) \int_V F_{L,\theta}^2 dV \right]^{1/2}. \quad (11)$$

It indicates transition of the dominant feedback on the flow from the currents induced by the Rossby wave to those induced by its subharmonic, leading to a 5-times increase in rms force amplitude. Similarly to induction term, large contributions to Lorentz force are given by interaction of electric currents induced by magnetic part of Rossby wave or subharmonic with the same magnetic mode, e.g., $(\nabla \times \mathbf{B}^{RW}) \times \mathbf{B}^{RW}$ and the mean magnetic field - e.g., $(\nabla \times \mathbf{B}^{SW}) \times \mathbf{B}^M$. A considerable contribution to Lorentz force arises from interaction of currents induced by the large-scale current, $\nabla \times \mathbf{B}^M$, and mean field \mathbf{B}^M . Similar behaviour is found in the radial and azimuthal components of the Lorentz force, except for $F_{l,\phi}$ where the interaction of the form $(\nabla \times \mathbf{B}^{SW}) \times \mathbf{B}^{SW}$ is the strongest, indicating potential mechanism of zonal flow enhancement \mathbf{u}_M in the transient regime. As for the interactions between the Rossby wave and the subharmonic, such as $\mathbf{u}^{SW} \times \mathbf{B}^{RW}$, $(\nabla \times \mathbf{B}^{RW}) \times \mathbf{B}^{SW}$, etc., these are active only during transitions between different unstable flow states, at $t \approx 1.4$ and $t \approx 2.0$.

5.2 Taylorization and Taylor-Proudman constraint

During the subharmonic state, both flow and magnetic field reconfigure so that their amplitude exhibits a maximum around the tangent cylinder (figure 3d), and strong gradients develop at high latitudes in its vicinity. To investigate the role of the tangent cylinder in the transition, we introduce two characteristic measures of force balance in the system, integrated over the curved cylindrical surface $C(s)$ of radius s , coaxial with the rotation axis. The first one, "Taylicity"

$$T_a = \frac{\left(s \int_{C(s)} [(\nabla \times \mathbf{B}) \times \mathbf{B}] \mathbf{e}_\phi dz d\phi \right)^2}{\langle B^2 \rangle^2}, \quad (12)$$

was proposed by Li et al. [9] to measure how well Taylor constraint and thus magnetostrophic force balance is satisfied (see section 1 for more details). In figure 6(a) we plot this quantity at different

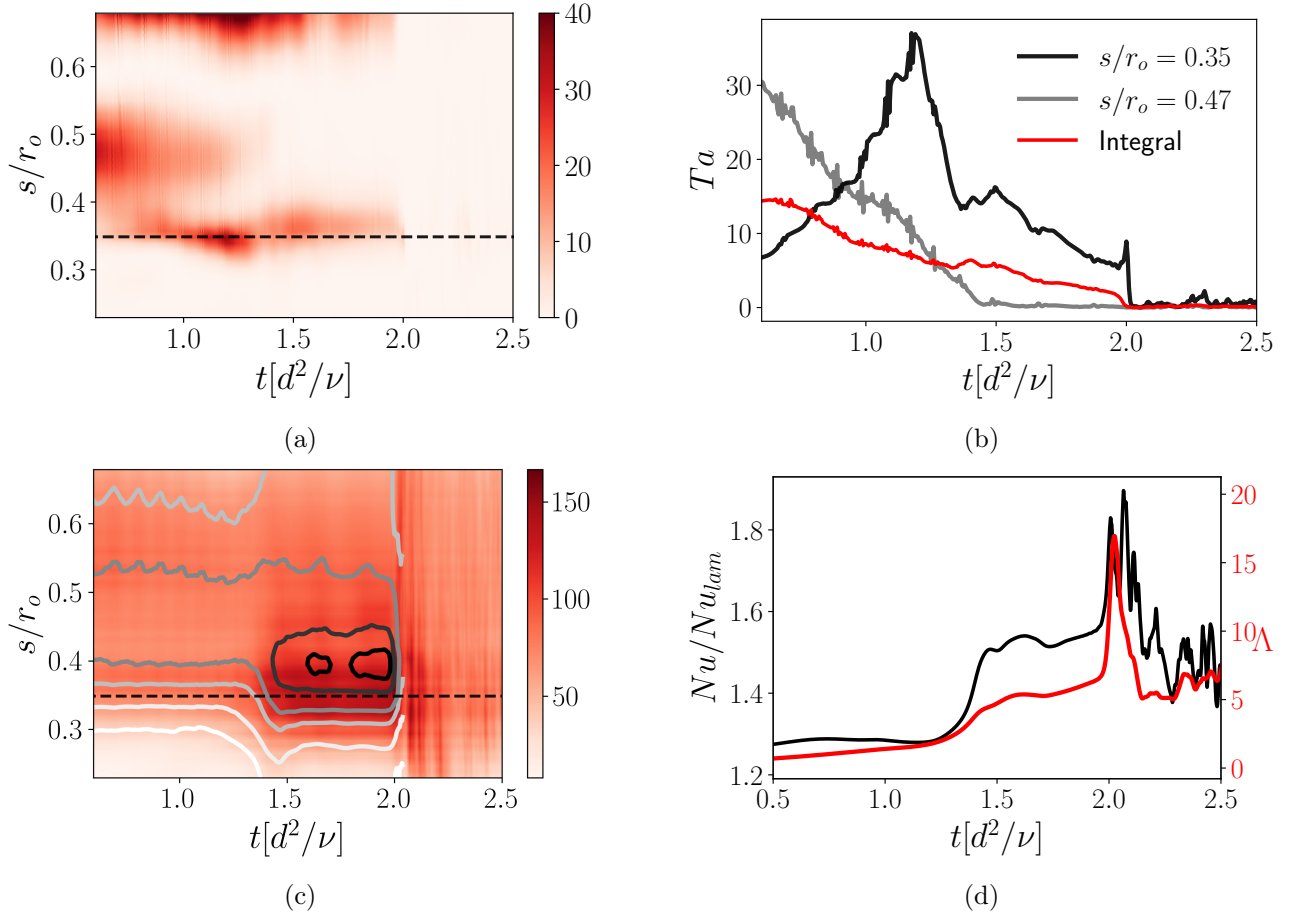


Figure 6: (a) Taylorization measure T_a as a function of cylindrical radius s and time. Dashed line indicates the tangent cylinder, $s/r_o = 0.35$. (b) T_a at $s/r_o = 0.35$ and $s/r_o = 0.47$, together with the integral over the radius s (in red). (c) In red: the distribution of velocity gradients $\int_{C(s)} |\partial u / \partial z| dz d\phi$, normalized by the surface area of $C(s)$. Grey contours denote the normalized integral for velocity, $\int_{C(s)} |u| dz d\phi$, at increasing levels of $[10, 25, 50, 70, 100, 118]$. (d) Nusselt number Nu at the bottom of the convective zone normalized with its laminar value Nu_{lam} (in black) and Elsasser number (in red). $Ra = 180$, initial conditions at $Ra = 160$.

cylindrical radii during transition. In the weak dynamo state, T_a is maximal in two regions: near the equator, where both magnetic field and stresses are very small, and around $s = 0.47r_o$. As the flow undergoes the subharmonic instability, this maximum moves towards the tangent cylinder, denoted by the dashed line. This result suggests that the subharmonic dynamo state is not in the magnetostrophic force balance. When the subharmonic state itself becomes unstable and chaotic strong-field dynamo sets in, T_a approaches zero both at the tangent cylinder and integrally, indicating that the dynamo is entering magnetostrophic force balance everywhere in the domain (figure 6). The azimuthal magnetic tension peaks at the tangent cylinder at about $t \approx 1.3$.

According to Taylor-Proudman theorem for hydrodynamic flows, axial velocity gradients should be zero in the limit of strong rotation, a constraint that is broken when magnetic tension enters the dominant force balance. Thus the second measure,

$$T_u(t, s) = 2d \frac{\int_{C(s)} |\partial \mathbf{u} / \partial z| dz d\phi}{\int_{C(s)} |\mathbf{u}| dz d\phi}, \quad (13)$$

compares characteristic velocity gradients along rotation axis z to the typical value of velocity as a function of time and cylindrical radius. Figure 6(c) shows the colormap of the integrated velocity gradients $\int_{C(s)} |\partial u / \partial z| dz d\phi$ as a function of time and s , together with the contours of velocity measure $\int_{C(s)} |u| dz d\phi$, both divided by the area $2\pi ds$ of each cylindrical surface $C(s)$. It appears that velocity

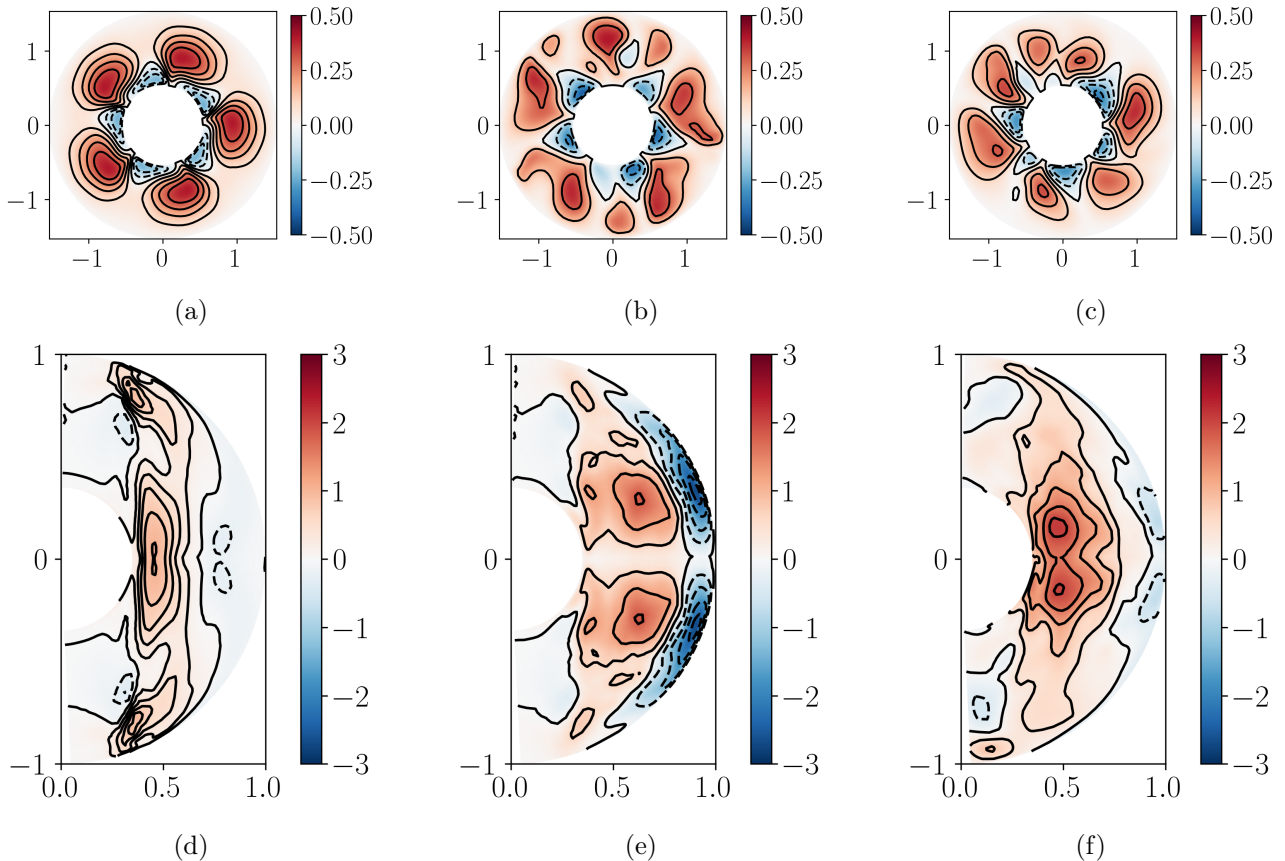


Figure 7: Instantaneous snapshots of (a-c) equatorial slices of temperature T ; (d-f) axisymmetric component of the field B_θ . (a,d) Subharmonic transient state before the runaway energy growth ($1.5 < t < 2.0$); (b,c) flow state at the peak of energy in figure 2(b), $t \approx 2.0$; (c,f) strong-field multimodal dynamo in chaotic state ($t > 2.0$). $Ra = 180$, initial conditions at $Ra = 160$.

increases in the vicinity of the tangent cylinder as the subharmonic mode develops. This result holds even when the mean zonal flow V_ϕ is subtracted, indicating the topological change in the flow structure accompanying transition. At the same time, velocity gradients develop a maximum at the tangent cylinder while the outer flow regions remain less affected. The magnitude of velocity is comparable to the magnitude of velocity gradients (see contour levels in figure 6c), resulting in nearly constant value of $T_u \approx 6$ throughout the entire transition. Thus, enhanced velocity gradients along z -axis, signalling less vertically constrained flow, do not necessarily indicate that the MAC force balance is achieved.

Finally, figure 6(d) illustrates the effect of these topological changes on two other diagnostic quantities, Nusselt number Nu and Elsasser number Λ ,

$$Nu = \frac{F_{heat}}{F_{cond}}, \quad \Lambda = \frac{B_{rms}^2}{2\Omega\rho\mu\eta}. \quad (14)$$

Nu , defined as a ratio between total heat flux F_{heat} and conductive heat flux F_{cond} , measures heat transport efficiency at the outer boundary r_o ; Λ measures the ratio of Lorentz to Coriolis force. While both 50% more efficient mode of convection and five time stronger fields are promoted by the subharmonic mode, it is when the subharmonic mode becomes unstable when these characteristics peak. After that, they relax back to the subharmonic levels in the strong-field state.

6 Run-away transition to chaos and strong dynamo

The transient subharmonic dynamo ends up in a rapid increase of kinetic and magnetic energy at about $t = 2$ (figure 2b). The contribution to the mean temperature profile and thus heat transfer also peak at this time (figure 4b). On the other hand, the subharmonic mode decays in magnetic field, together

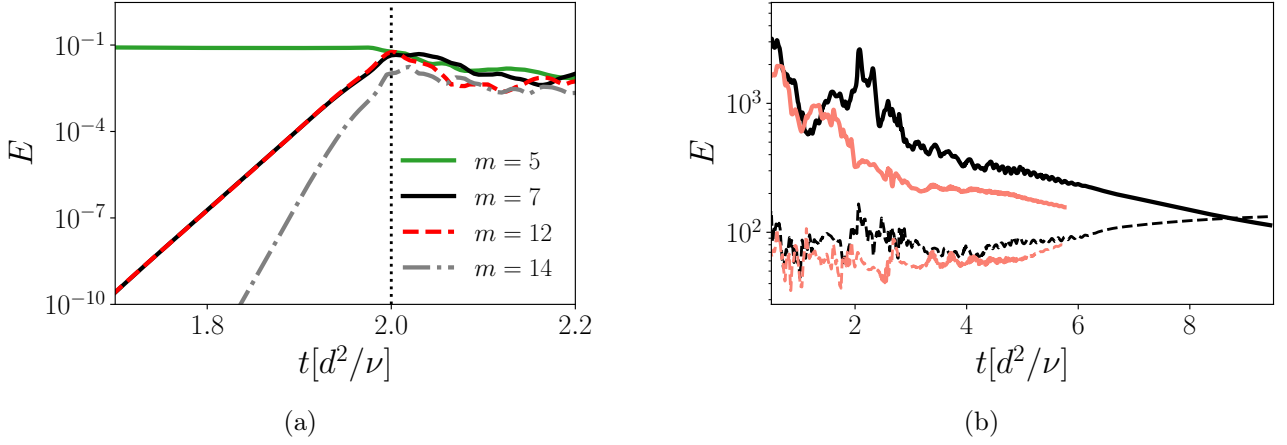


Figure 8: (a) Evolution of energy in different azimuthal structures of magnetic field during and after the subharmonic state. Black solid line, $m = 7$, green solid line, $m = 5$, dashed, $m = 12$, dashdotted, $m = 14$. Vertical dotted line represents transition to chaos as in figure 2(b). $Ra = 170$, initial conditions at $Ra = 160$. (b) Decay of the strong dynamo and inverse transition to the weak regime, $Ra = 140$ (in black, initial condition at $Ra = 160$) and $Ra = 130$ (initial condition at $Ra = 150$, in red).

with the mean magnetic modes and zonal flows (figure 4a,b). This run-away process is much faster than the growth of the subharmonic mode, and is followed by its breakdown into a turbulent strong-field dynamo state. The resulting axisymmetric dipolar field in the strong-field regime (figure 2c, right) resembles this of the subharmonic mean-field mode (figure 3b, middle), although the regions of the strongest magnetic field are no longer located at the tangent cylinder.

To understand better this transition, we follow the evolution of the dynamo energy spectra in time, here using the spherical harmonic representation employed in PaRoDy [27]. During the weak and the transient regimes, the energy is contained primarily in the azimuthal mode of $m = 5$, with a relatively simple flow structure (see temperature snapshots in figure 7a). In the transient regime, however, the subharmonic state allows to transfer energy to the rest of azimuthal wavenumbers. Figure 8(a) illustrates this process on the azimuthal structures of $m = 7$ and $m = 12$, which exhibit the fastest exponential growth of $\sigma_r = 33$ from nearly zero initial energy. In fact, all the azimuthal wave numbers are excited, some of them with the same growth rate of $m = 7$, and some of them like $m = 14$ growing two times faster, $\sigma_r \approx 65$. Their growth seems to be determined by secondary quadratic interactions of the first group, and their energy remains smaller at all times than the energy of the triad $m = (5, 7, 12)$. When $m = 7$ and $m = 12$ enter in equipartition with the subharmonic mode at $t \approx 2$, the total flow energy peaks (figure 2b), indicating a triadic resonance of the three structures. Only then the presence of $m = 7$ and $m = 12$ becomes apparent in the dynamo snapshots, which show convective rolls visibly splitting in half and moving outwards in the equatorial plane (figure 7b). Small flow scales imply larger dissipation, and so this flow configuration is highly unstable. Immediately after $t = 2$, the energy of $m = 12$ decays and the flow relaxes to a turbulent state still dominated by subharmonic-like structure, with contribution of $m = 7$ and lower-order azimuthal modes (figure 7c). This is when the energy fluctuations develop in figures 2(b), 8(a), and the dynamo becomes turbulent.

Topological changes in the flow result in respective adjustment of the magnetic field. Figures 7(d-f) shows the latitudinal component of axisymmetric magnetic field $\langle B_\theta \rangle_\phi$, for illustration of dipolar field evolution. During the subharmonic transient, the maximum intensity of the field is observed at the tangent cylinder, and is correlated with the strong prograde zonal flow (figure 3b, right). When convective structures are expelled outwards during triadic resonance, magnetic flux is also expelled from the tangent cylinder towards the outer sphere (figure 7e). The zonal flow (not shown here for brevity) is disrupted and considerably weakens in amplitude; the prograde jet bends towards the equator at high latitudes, constraining the location of the retrograde flow to the equatorial area. As $m = 12$ mode decays, magnetic structures move back to the bulk of the domain (figure 7f), and the zonal flow reconfigures to a state similar to the subharmonic, although a slight bent towards the equator remains in the zonal flow (figure 2d, right).

7 Discussion and conclusions

In this work, we analysed subcritical transitions from the weak to strong dynamo using a novel data-driven method of Dynamic Mode Decomposition. Our results show that this transition takes place through a succession of two unstable states. The first one is dominated by a subharmonic mode of convective Rossby wave from the weak-field regime and features a strong prograde zonal flow near the tangent cylinder. The dynamo is able to evolve around this state for considerable amount of time, independently of Ra . In this state, convective Rossby wave remains weak, and both the flow and field exhibit topological changes. The local maxima of dipolar axisymmetric magnetic field shift from the area inside the tangent cylinder to the tangent cylinder itself. A possible explanation for this phenomenon is that in the weak-field regime magnetic flux is generated by convective columns in the bulk and is transported by them inside the tangent cylinder. With strong shear at the tangent cylinder, this process is inhibited because the azimuthal jet transforms inward radial magnetic flux into toroidal, and prevents the accumulation of the net magnetic flux near the axis of rotation. In the strong-field regime, the flow is no longer constrained vertically at the tangent cylinder, and magnetic structures generated in the bulk of the flow are able to penetrate inside the tangent cylinder; nevertheless local magnetic maxima remain weak there, indicating that the shear is still dynamically active (compare figures 2c,d). Note that the axisymmetric dynamo configuration remains predominantly dipolar despite developing turbulence. In addition, we analysed the contribution of the identified mean, Rossby and subharmonic DMD modes to the generation of induction and Lorentz forces in the system during the weak and subharmonic regimes. The dominant nonlinear interactions throughout the transition are those of the subharmonic and the mean flow: (M, SW, SW) and (SW, SW, M) (figure 5). Our results suggest that the mechanism generating the dynamo changes from α^2 to $\alpha - \Omega$ as the dynamo enters the subharmonic regime.

The subharmonic state is followed by a runaway growth of the flow energy in azimuthal modes $m = 7$ and $m = 12$, growing exponentially and entering triadic resonance with quasi-steady subharmonic mode of $m = 5$. The resonance is accompanied by expulsion of the dipolar magnetic field away from the tangent cylinder. After the decay of small-scale mode $m = 12$, the dynamo relaxes to a distorted chaotic state with the flow and field structure similar to that of the subharmonic (figure 7d-f). Subsequent order-of-magnitude decrease in surface-averaged azimuthal magnetic stresses indicates that the dominant magnetostrophic balance was achieved in the strong-field turbulent state but not in the subharmonic regime, where magnetic stresses are large at the tangent cylinder (figure 6a,b). In table 1 we compare the growth rates of the resonance modes and their quadratic interactions with the growth rates of convectively unstable modes, computed with small perturbations as initial conditions and nonlinear feedback terms switched off in equations (1). The dominant wavenumbers of convectively unstable modes are smaller-scale structures of $m = 7, 8$, and 9 , comparable to the ones responsible for triadic resonance. Although the hydrodynamic instability develops faster than the resonance or secondary modes, the growth rates of both are comparable and are distinctly different from much slower growth rates of the kinematic weak dynamo and the subharmonic mode itself. This suggests that the subharmonic state with its slightly increased magnetic field facilitates the growth of hydrodynamically unstable convective modes that are otherwise inhibited by magnetic field, favouring large-scale structures. The differences in the growth rates could arise due to the fundamental changes in the base flow state, with a flatter mean temperature profile and non-zero mean magnetic field. Similar lowering of convective threshold in the presence of moderate magnetic fields was observed recently in simulations of magnetoconvection [36].

During the inverse transition from the strong to weak-field dynamo, when Ra is decreased beyond stability of the strong-field branch (figure 2a), the flow does not revisit described above flow states (figure 8b). Instead, the inverse transition takes place through a gradual relaxation of chaos in previously excited azimuthal modes, while the dominant convective mode grows as the only one able to extract energy from the mean temperature profile. The existence of the two unstable states is constrained by the region of bi-stability in figure 2(a), where the two locally attracting weak- and strong-field states serve as boundaries. The chaotic strong-field solution decays when Ra is low and outside of this region, so the only remaining attractors for these runs are either the weak-field dynamo or purely non-magnetic convective states at even lower Ra . These unstable states could be found exactly using

Ra	Convection	Weak dynamo	Subharmonic	Resonance modes	Secondary modes
160	190	0.436			
170	208	0.434	2.174	33.243	65.139

Table 1: Estimated growth rates of several instabilities in the dynamo flow. From the left to the right: hydrodynamic convective instability (dominant azimuthal wavenumbers $m = 7, 8, 9$), kinematic growth of the weak magnetic field due to it, growth rate of the subharmonic mode ($m = 5$), growth of dominant resonance modes $m = 7$ and $m = 12$, and their secondary nonlinear quadratic interactions (i.e., $m = 14$) at $Re = 170$.

adjoint techniques [37] or edge-tracking bisection method [38]. Furthermore, the distribution of the energy as a function of spherical degree l (not shown here for brevity) remains similar through the whole transition. Therefore, the dynamically important direction of transition to strong-field dynamo is azimuthal angle ϕ , not latitude θ . Described here modal structures span the whole dynamical landscape of this system; in the future work, we aim to construct data-driven reduced-order models of such transitions using Sparse Identification of Nonlinear Dynamics [39] or Galerkin methods [40].

Subcritical dynamos like those reported here and in previous works of Dormy [19], Petitdemange [20] are of particular interest for understanding the evolution of planetary magnetic fields. Our analysis shows that the physical origin of this behaviour is related to sufficiently strong magnetic field being able to induce subharmonic instability of the dynamo on the weak-field branch. In the future, we will focus on such transitions in parameter regimes relevant for planetary dynamos at lower E numbers. The weak-field branch in this case corresponds to multipolar dynamos [20]; however, the corresponding transition scenario can share similar features. The physical processes described here give rise to a turbulent dynamo dominated by a magnetostrophic balance at large scales, and may also play a role in the formation of dipole-dominated magnetic fields during magnetic reversals.

Open Research Section

All the data supporting this work, including energy time series, flow and magnetic field snapshots, DMD modes, their eigenvalues and instantaneous coefficients, are available at repository Zenodo via DOI 10.5281/zenodo.11164961 with CC BY 4.0 license [41]. The full series of raw flow snapshots comprize tens of gigabytes of data and will be made available on demand to the corresponding author.

Acknowledgements

This work has received funding from the European Union’s Horizon 2020 research and innovation programme under the Marie Skłodowska-Curie grant agreement No 890847. It was partly supported by funding from the French program 'PROMETHEE' managed by Agence Nationale de la Recherche and from "Visiting Fellowship" managed by Observatoire de Paris-PSL. This study used the HPC resources of MesoPSL financed by the Région île-de-France and the project EquipMeso (reference ANR-10-EQPX-29-01) of the program Investissements d’Avenir, supervised by the Agence Nationale pour la Recherche.

References

- [1] K. Moffatt, *Magnetic Field Generation in Electrically Conducting Fluids*. Cambridge University Press, 1978.
- [2] N. Schaeffer, D. Jault, H.-C. Nataf, and A. Fournier, “Turbulent geodynamo simulations: a leap towards earth’s core,” *Geophysical Journal International*, vol. 211, no. 1, pp. 1–29, 2017.
- [3] N. Gillet, D. Jault, E. Canet, and A. Fournier, “Fast torsional waves and strong magnetic field within the earth’s core,” *Nature*, vol. 465, no. 7294, pp. 74–77, 2010.

- [4] C. C. Finlay, N. Gillet, J. Aubert, P. W. Livermore, and D. Jault, “Gyres, jets and waves in the earth’s core,” *Nature Reviews Earth & Environment*, vol. 4, no. 6, pp. 377–392, 2023.
- [5] K. Hori, C. A. Jones, A. Antuñaño, L. N. Fletcher, and S. M. Tobias, “Jupiter’s cloud-level variability triggered by torsional oscillations in the interior,” *Nature Astronomy*, vol. 7, no. 7, pp. 825–835, 2023.
- [6] M. Dumberry and J. Bloxham, “Torque balance, Taylor’s constraint and torsional oscillations in a numerical model of the geodynamo,” *Physics of the Earth and Planetary Interiors*, vol. 140, no. 1-3, pp. 29–51, 2003.
- [7] J. Taylor, “The magneto-hydrodynamics of a rotating fluid and the earth’s dynamo problem,” *Proceedings of the Royal Society of London. Series A. Mathematical and Physical Sciences*, vol. 274, no. 1357, pp. 274–283, 1963.
- [8] D. Fearn and M. Rahman, “Evolution of non-linear α 2-dynamos and Taylor’s constraint,” *Geophysical & Astrophysical Fluid Dynamics*, vol. 98, no. 5, pp. 385–406, 2004.
- [9] K. Li, A. Jackson, and P. W. Livermore, “Taylor state dynamos found by optimal control: axisymmetric examples,” *Journal of Fluid Mechanics*, vol. 853, pp. 647–697, 2018.
- [10] G. A. Glatzmaiers and P. H. Roberts, “A three-dimensional self-consistent computer simulation of a geomagnetic field reversal,” *Nature*, vol. 377, no. 6546, pp. 203–209, 1995.
- [11] C. Jones, “A dynamo model of Jupiter’s magnetic field,” *Icarus*, vol. 241, pp. 148–159, 2014.
- [12] T. Gastine, J. Wicht, L. Duarte, M. Heimpel, and A. Becker, “Explaining Jupiter’s magnetic field and equatorial jet dynamics,” *Geophys. Res. Lett.*, vol. 41, no. 15, pp. 5410–5419, 2014.
- [13] J. Aubert, “Approaching Earth’s core conditions in high-resolution geodynamo simulations,” *Geophysical Journal International*, vol. 219, no. Supplement_1, pp. S137–S151, 2019.
- [14] P. Davidson, “Scaling laws for planetary dynamos,” *Geophysical Journal International*, vol. 195, no. 1, pp. 67–74, 2013.
- [15] J. Aubert, T. Gastine, and A. Fournier, “Spherical convective dynamos in the rapidly rotating asymptotic regime,” *Journal of Fluid Mechanics*, vol. 813, pp. 558–593, 2017.
- [16] R. K. Yadav, T. Gastine, U. R. Christensen, S. J. Wolk, and K. Poppenhaeger, “Approaching a realistic force balance in geodynamo simulations,” *Proceedings of the National Academy of Sciences*, vol. 113, no. 43, pp. 12065–12070, 2016.
- [17] R. J. Teed and E. Dormy, “Solenoidal force balances in numerical dynamos,” *Journal of Fluid Mechanics*, vol. 964, p. A26, 2023.
- [18] R. Hollerbach, “On the theory of the geodynamo,” *Physics of the Earth and Planetary Interiors*, vol. 98, no. 3-4, pp. 163–185, 1996.
- [19] E. Dormy, “Strong-field spherical dynamos,” *J. Fluid Mech.*, vol. 789, pp. 500–513, 2016.
- [20] L. Petitdemange, “Systematic parameter study of dynamo bifurcations in geodynamo simulations,” *Phys. Earth Planet. In.*, vol. 277, pp. 113–132, 2018.
- [21] U. R. Christensen and J. Aubert, “Scaling properties of convection-driven dynamos in rotating spherical shells and application to planetary magnetic fields,” *Geophysical Journal International*, vol. 166, no. 1, pp. 97–114, 2006.
- [22] M. D. Menu, L. Petitdemange, and S. Galtier, “Magnetic effects on fields morphologies and reversals in geodynamo simulations,” *Phys. Earth Planet. In.*, vol. 307, p. 106542, 2020.

- [23] K. Hori and J. Wicht, “Subcritical dynamos in the early mars’ core: Implications for cessation of the past martian dynamo,” *Physics of the Earth and Planetary Interiors*, vol. 219, pp. 21–33, 2013.
- [24] P. J. Schmid, “Dynamic mode decomposition and its variants,” *Annu. Rev. Fluid Mech.*, vol. 54, pp. 225–254, 2022.
- [25] A. Guseva, “Data-driven scale identification in oscillatory dynamos,” *Monthly Notices of the Royal Astronomical Society*, vol. 528, no. 2, pp. 1685–1696, 2024.
- [26] A. Guseva and S. M. Tobias, “Transition to chaos and modal structure of magnetized taylor–couette flow,” *Philosophical Transactions of the Royal Society A*, vol. 381, no. 2243, p. 20220120, 2023.
- [27] E. Dormy, P. Cardin, and D. Jault, “Mhd flow in a slightly differentially rotating spherical shell, with conducting inner core, in a dipolar magnetic field,” *Earth and Planetary Science Letters*, vol. 160, no. 1-2, pp. 15–30, 1998.
- [28] B. O. Koopman, “Hamiltonian systems and transformation in hilbert space,” *Proceedings of the National Academy of Sciences*, vol. 17, no. 5, pp. 315–318, 1931.
- [29] J. H. Tu, C. W. Rowley, D. M. Luchtenburg, S. L. Brunton, and J. N. Kutz, “On dynamic mode decomposition: Theory and applications,” *Journal of Computational Dynamics*, vol. 1, no. 2, pp. 391–421, 2014.
- [30] H. Arbabi and I. Mezic, “Ergodic theory, dynamic mode decomposition, and computation of spectral properties of the koopman operator,” *SIAM Journal on Applied Dynamical Systems*, vol. 16, no. 4, pp. 2096–2126, 2017.
- [31] P. J. Schmid, “Dynamic mode decomposition of numerical and experimental data,” *Journal of fluid mechanics*, vol. 656, pp. 5–28, 2010.
- [32] M. R. Jovanović, P. J. Schmid, and J. W. Nichols, “Sparsity-promoting dynamic mode decomposition,” *Physics of Fluids*, vol. 26, no. 2, p. 024103, 2014.
- [33] K. Moffatt and E. Dormy, *Self-exciting fluid dynamos*. Cambridge University Press, 2019, vol. 59.
- [34] M. Schrunner, K.-H. Rädler, D. Schmitt, M. Rheinhardt, and U. R. Christensen, “Mean-field concept and direct numerical simulations of rotating magnetoconvection and the geodynamo,” *Geophysical & Astro Fluid Dynamics*, vol. 101, no. 2, pp. 81–116, 2007.
- [35] M. Schrunner, L. Petitdemange, and E. Dormy, “Dipole collapse and dynamo waves in global direct numerical simulations,” *Astrophys. J.*, vol. 752, no. 2, p. 121, 2012.
- [36] S. J. Mason, C. Guervilly, and G. R. Sarson, “Magnetoconvection in a rotating spherical shell in the presence of a uniform axial magnetic field,” *Geophysical & Astrophysical Fluid Dynamics*, vol. 116, no. 5-6, pp. 458–498, 2022.
- [37] P. M. Mannix, Y. Ponty, and F. Marcotte, “Systematic route to subcritical dynamo branches,” *Physical Review Letters*, vol. 129, no. 2, p. 024502, 2022.
- [38] A. Guseva, R. Hollerbach, A. P. Willis, and M. Avila, “Azimuthal magnetorotational instability at low and high magnetic prandtl numbers,” *Magnetohydrodynamics*, vol. 53, no. 1, pp. 25–34, 2017.
- [39] S. L. Brunton, J. L. Proctor, and J. N. Kutz, “Discovering governing equations from data by sparse identification of nonlinear dynamical systems,” *P. Natl. Acad. Sci. USA*, vol. 113, no. 15, pp. 3932–3937, 2016.
- [40] B. R. Noack and H. Eckelmann, “A low-dimensional galerkin method for the three-dimensional flow around a circular cylinder,” *Physics of Fluids*, vol. 6, no. 1, pp. 124–143, 1994.

- [41] A. Guseva, "Supplementary materials for the manuscript "Run- away transition to turbulent strong-field dynamo"," May 2024. [Online]. Available: <https://doi.org/10.5281/zenodo.11164961>